

Research papers

Hydro-mechanical coupling in the shallow crust – Insight from groundwater level and satellite radar imagery in a mining area



Zheming Shi^{a,b}, Xie Hu^a, Chi-Yuen Wang^{a,*}

^a Department of Earth & Planetary Science, University of California, Berkeley, United States

^b MOE Key Laboratory of Groundwater Circulation and Environment Evolution, China University of Geosciences, Beijing 100083, China

ARTICLE INFO

This manuscript was handled by Marco Borga, Editor-in-Chief, with the assistance of Yong-qiang Zhang, Associate Editor

Keywords:

Hydro-mechanical coupling
Tidal response
Water level
InSAR
Mining

ABSTRACT

The hydro-mechanical coupling in the shallow crust influences both geological processes such as earthquakes and landslides and anthropogenic processes such as induced seismicity and mining-produced subsidence. Yet there have been few direct field observation to illustrate how the hydraulic and the mechanical processes are coupled. In this study we use continuous water level data from wells and ground deformation data over a large area ($>71 \text{ km}^2$) of active coal mining in NW China to examine hydro-mechanical coupling in the shallow crust. We present detailed analysis of the tidal response of groundwater and surface deformation from radar remote sensing in an actively and intensely mined area, and we show that the phase shift of the tidal response of water level may respond significantly to mining disturbances when the excavation workface was many hundred meters to $>1 \text{ km}$ away, whereas significant ground deformation and water-level drops occurred only when the workface came much closer to the wells. Water level and tidal response recovered after the workface moved away but the subsidence is permanent. We suggest that the permeability of the mined crust may be controlled by narrow conductive fractures that open and close in response to deviatoric stresses, while large ground deformation and water-level drops may be controlled by larger fractures and faulting. One possibility is the release of the deviatoric stresses in the wall rocks by faulting, may have allowed the conductive fractures to close and the water level and its tidal response to recover after the workface moved away. Another possible mechanism is the mobilization of precipitates in clogged fractures by dynamic waves associated with mining-induced seismicity, which may change the permeability of fractures. More studies are warranted for a better understanding of the hydro-mechanical coupling during longwall mining.

1. Introduction

Hydro-mechanical coupling, i.e., the interaction between rock deformation and pore water in crustal rocks (e.g., Stephansson, 2003), is important for understanding many geological and anthropogenic processes, including landslides, subsidence, induced seismicity, and ground deformation due to wastewater injection (Armand et al., 2014; Shirzaei et al., 2016; Zhai et al., 2019). Mining induced hydrogeological changes have been documented for decades (Booth, 2002; Booth and Spande, 1992; Jung et al., 2007; Sheng et al., 2010; Zhang et al., 2010), but there have been few continuous field observations to illustrate how the hydraulic and the mechanical processes may be coupled. The relationship between permeability and deformation during mining remains poorly understood and there is little confidence in quantitative assessments of the impacts of mining on groundwater (Adhikary and Guo, 2015; Day

et al., 2020; Feng et al., 2007; McNally and Evans, 2007). Continuous field monitoring of changes in hydraulic properties during deformation is critical to constrain numerical and conceptual models (Bai and Elsworth, 1995; David et al., 2017) and to evaluate the potential impact of mining on groundwater resources (Liu and Elsworth, 1997), which is especially important for understanding the impact of mining in arid and semi-arid regions where the groundwater resource is scarce and the ecological environment is vulnerable (Booth, 2002).

In this study, we report continuous monitoring of groundwater levels in wells and surface deformation from radar remote sensing during 2016–2018 over a large area ($>71 \text{ km}^2$) of active coal mining in northwestern China (Fig. 1a) to study the evolution of hydro-mechanical coupling between groundwater and deformation. We present detailed analysis of the tidal response of groundwater in an actively and intensively mined area. We show that the phase shift of the tidal response of

* Corresponding author.

E-mail address: chiyuen@berkeley.edu (C.-Y. Wang).

water level is by far the most sensitive indicator of changes in hydro-mechanical coupling. Water level and its tidal response in the well recovered after the workforce moved away, suggesting that the deviatoric stresses that control the opening and closing of narrow conductive fractures may have been released.

This study differs from previous studies of pump tests before and

after mining (Booth and Spande, 1992), numerical simulations (Adhikary and Guo, 2015), laboratory experiments (Meng et al., 2016) and underground measurements (Armand et al., 2014) in that we study the continuous changes of water level, its tidal response and the ground deformation in an area of progressive active mining. It also differs from the study of David et al (2017) in that we focus on changes in the hydro-

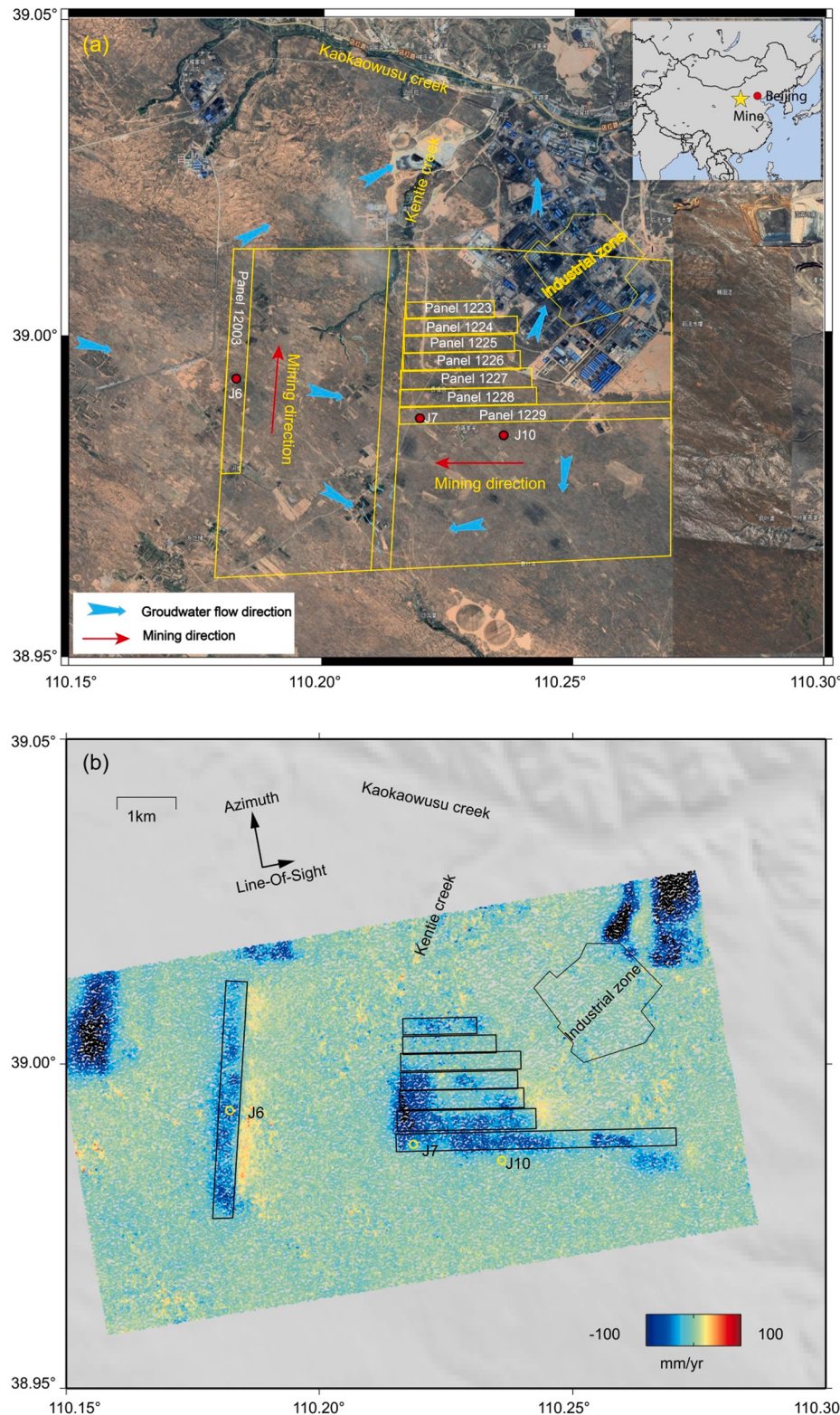


Fig. 1. (a) Location map of the coalfield, wells and excavated panels. (b) Vertical surface displacement rate derived from ascending Sentinel-1 InSAR data (September 2016 to March 2019). J6, J7 and J10 are three groundwater wells over the coal seam.

mechanical coupling during progressive mining from analysis of the tidal response of water level and satellite radar imagery, while David et al. (2017) focused on evaluating the changes in storage with mining from analysis of the barometric efficiency. In addition, our study provides a novel joint time-series analysis of high-frequency water level data and remotely sensed ground displacement data, which can also be used in other areas such as wastewater injection, induced seismicity and dynamic land subsidence in general.

2. Observation

2.1. Geological settings

The 71.2-km² Ningtiaota coalfield is located in the Shannxi Province in northern China (Fig. 1a). The coalfield strata are gently inclined at $\sim 1^\circ$ to the northeast as a monocline (Xue et al., 2010; Ding et al., 2016). Underground coal mining using the longwall mining method has been in operation since 2013. About 11 longwall panels (Fig. 1a), typically 2–4 km in length, ~ 300 m in width and ~ 4 m in height (Fig. 1b), have been excavated at different times. Table 1 shows the monthly advancement of each panel provided by the mining company.

The overburden strata above the extracted coal seam (Fig. 2) consist of the Jurassic Yanan group and Zhiluo group, the Neogene Pliocene Baode Group, the Middle Pleistocene Lishi Group, and Quaternary alluvium and eolian sand, with a total thickness between 140 and 200 m.

Three aquifers are contained in the coal field; the lowest aquifer in the Yan'an siltstone has a relatively low hydraulic conductivity ($\sim 2 \times 10^{-4}$ m/d); the middle aquifer in the Zhiluo fractured and weathered rocks is the major aquifer with a range of hydraulic conductivities

between 0.05 and 12.35 m/d; and the uppermost aquifer in the Upper Pleistocene and Quaternary alluvium is unconfined. Groundwater in the unconfined aquifer is recharged mainly by local precipitation but shows evidence of exchange with groundwater in the confined aquifers below. The general pattern of groundwater flow is shown by arrows in Fig. 1a (Huang et al. 2018).

2.2. InSAR analysis and surface subsidence

InSAR (interferometric SAR) methods have been increasingly used to study ground deformation associated with processes such as aquifer recharge/discharge, tailings settlement, oil/gas extraction, coal fires, and landslides (e.g., Hu et al., 2017, 2018; Shirzaei et al., 2016). Here we relied on one ascending track of Sentinel-1 (no descending data available) to monitor ground deformation in the coal mining area. We applied small multilooks (1 in azimuth and 4 in range, i.e., ~ 14 m pixel spacing on the ground) to generate the interferograms in order to best preserve drastic deformation, i.e., condensed fringes, in localized areas (Hu et al., 2020). Here we performed time-series analysis using a stack of 108 interferograms with less than 24-day temporal intervals to derive the evolution of surface movements between September 2016 and March 2019 (Fig. 3). The initial interferograms represent a combination of the ground deformation, surface topography, and artifacts from the atmosphere, satellite orbit, etc. We used 90-m-resolution Shuttle Radar Topography Mission (SRTM) Digital Elevation Model (DEM) to simulate the topographic phase component. We also constrained a spatial ramp fitted by the bilinear polynomial function. To be rational, we performed the fitting on areas out of the active mine sites. Thereafter, we applied the derived bilinear coefficients for the entire region to approximate the long-wavelength artifacts such as that from the atmospheric phase screens and orbits (e.g., Hu et al., 2018). We resolved the time-series displacements based on the singular value decomposition using the corrected unwrapped interferograms. Note that the interferograms are not fully connected, with brief gaps in the summer due to intense rainfall and loss of coherence, and we assumed no motions during these gaps for a conservative velocity estimate. We converted the radar line-of-sight measurements to the vertical direction assuming that horizontal motion is negligible. Fig. 1b shows the cumulative vertical surface displacement from 2016 to 2019 and Fig. 4d shows the time series of vertical displacement at the three wells. Fig. 5 shows the time-series displacement maps which vividly capture ground subsidence during the progression of underground workface (Table 1).

In general, the vertical displacements change smoothly with time (Fig. 4d), partly due to the relatively coarse temporal sampling of the SAR scenes. The ground near the J6 well (Fig. 4d, J6), for example, began to subside when the workface approached the well at a distance of ~ 300 m; subsidence continued when the workface passed through the well, with a total subsidence of 120 mm when the workface advanced ~ 900 m beyond the well. No perceptible subsidence occurred thereafter.

Heavy seasonal rain in the summer of 2017 caused loss of InSAR coherence near the J7 well (Fig. 4d). By utilizing the August 3–15 and September 20–October 2 interferograms, however, a clear and drastic displacement was identified when the workface was directly beneath the well (indicated by a red vertical dashed line in Fig. 4d, J7), which may indicate faulting. The ground continued to subside until May 2018 with a total subsidence of at least 100 mm during the course of ~ 1 year. The actual displacement may be even larger, given that the displacement during the interferogram gaps was assumed zero. The J10 well was not situated directly above an excavated panel and thus the total subsidence near the well (~ 30 mm, Fig. 4d, J10) is much smaller than that near the other two wells. Overall, the averaged standard deviation of the cumulative displacements measured within a distance of 30 m from wells J6, J7, and J10 are 4.5 mm, 5.1 mm, and 8.4 mm, respectively. Slight uplift appears along the south-north advancing panel (#12003, Fig. 1b), which may be an artifact because it occurs only on one side of the panel instead of on both sides. Subsidence along the axis of the panel caused

Table 1
Underground progression of the workface.

Relative distance of J7 to S1229 workface		Relative distance of J10 to S1229 workface		Relative distance of J6 to S12003 workface	
Date	Relative distance to the work face	Date	Relative distance to the work face	Date	Relative distance to the work face
Jun-16	-2962	Jun-16	-1412	Oct-17	-1618
Jul-16	-2954	Jul-16	-1404	Nov-17	-1382
Aug-16	-2939	Aug-16	-1389	Dec-17	-1171
Sep-16	-2919	Sep-16	-1369	Jan-18	-870
Oct-16	-2771	Oct-16	-1221	Feb-18	-538
Nov-16	-2447	Nov-16	-897	Mar-18	-227
Dec-16	-2193	Dec-16	-643	Apr-18	-98
Jan-17	-1895	Jan-17	-345	May-18	191
Feb-17	-1572	Feb-17	-22	Jun-18	536
Mar-17	-1277	Mar-17	273	Jul-18	985
Apr-17	-977	Apr-17	573	Aug-18	1427
May-17	-712	May-17	838		
Jun-17	-401	Jun-17	1149		
Jul-17	-152	Jul-17	1398		
Aug-17	39	Aug-17	1589		
Sep-17	227	Sep-17	1777		
	17		17		

*J6, J7 and J10 are the three groundwater monitoring wells located in three different workfaces.

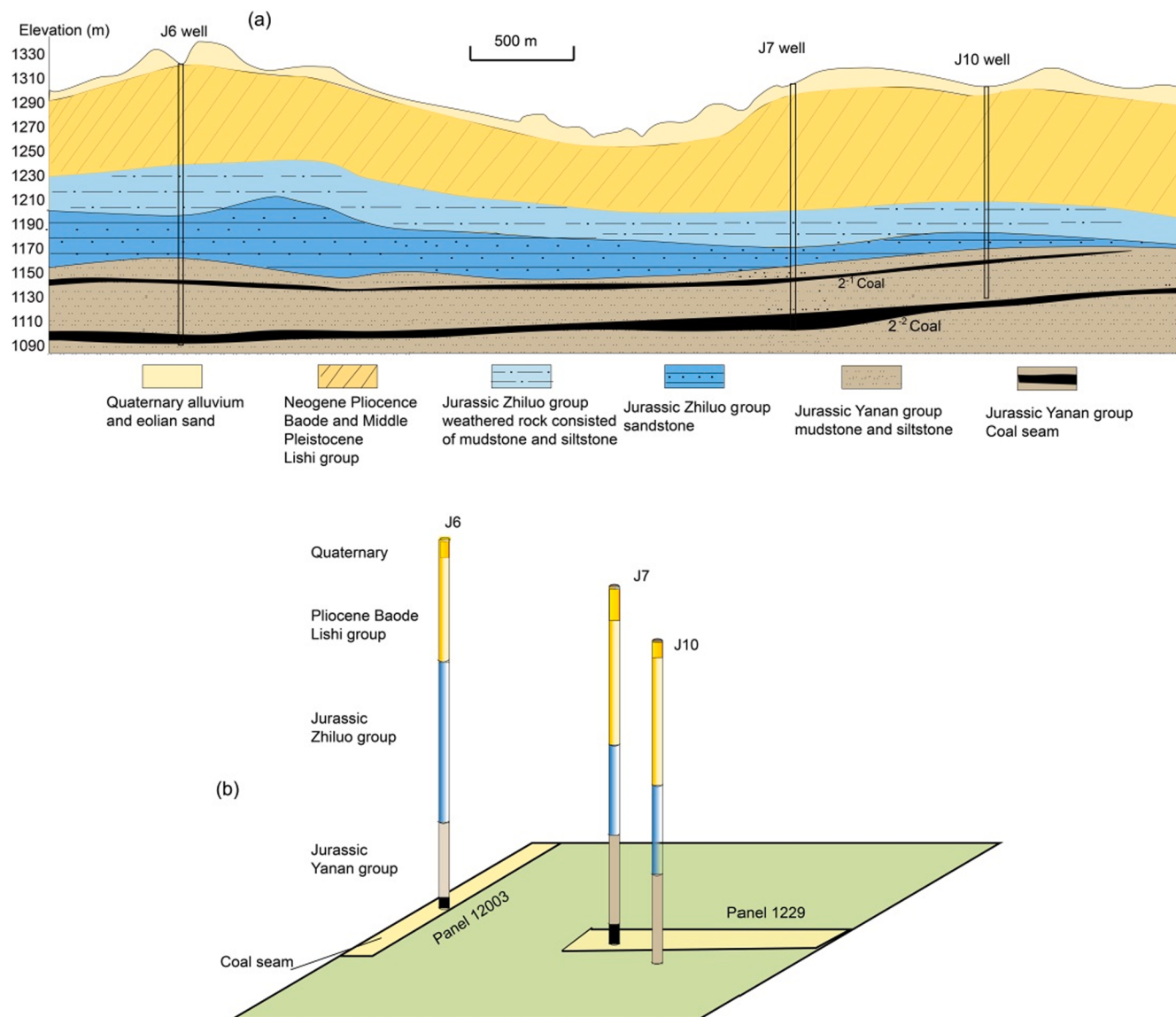


Fig. 2. (a) Geologic cross section and relative groundwater monitoring wells (J6, J7, and J10) positions; (b) 3D view of the spatial relationship between the wells and the excavated panels.

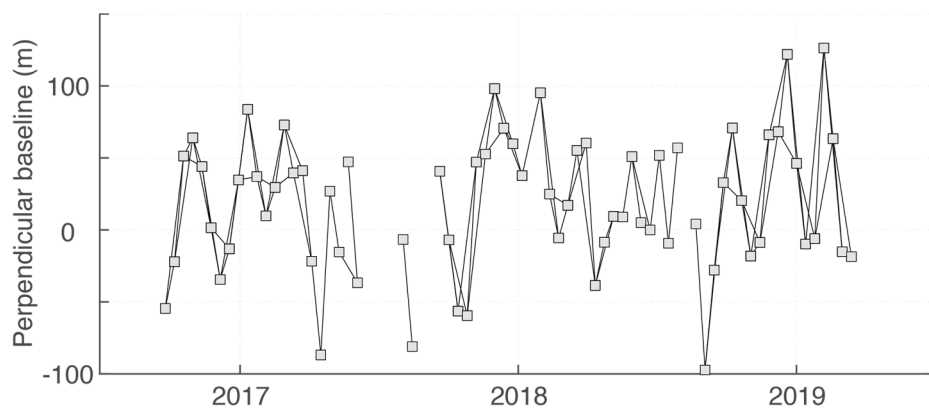


Fig. 3. InSAR baseline information.

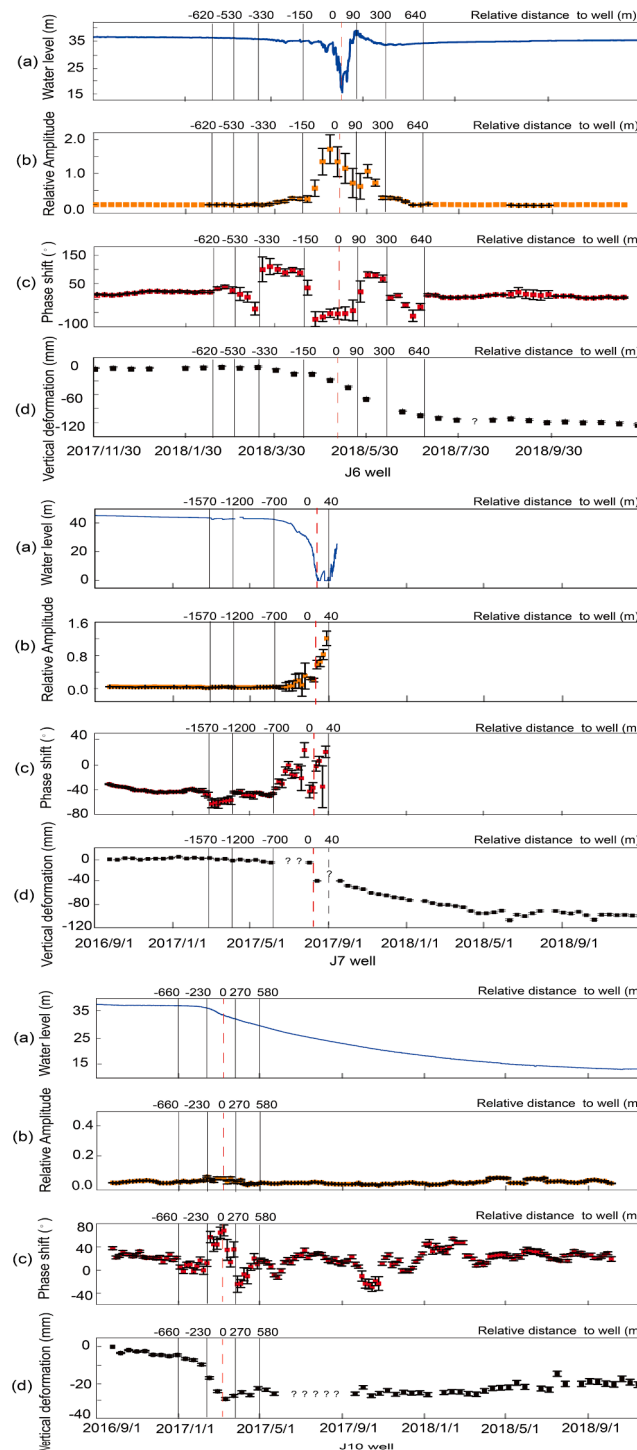


Fig. 4. Time-dependent changes in the J6 well, the J7 well and the J10 well of (a) water level, (b) amplitude ratio of water-level's response to the M2 tide, (c) phase shift of water-level's response to the M2 tide, and (d) ground subsidence. Question mark in the figures means uncertainty during the summer season. The dash line indicate the workface reached to the groundwater wells, while the vertical lines indicate the relative distance of the workface to the groundwater wells.

the margins to lose support and to move sideways towards the center. Therefore, the western margin moved to the east, away from the sensor in the ascending SAR satellite trajectory, and the eastern side moved to the west, toward the sensor, causing the apparent one-side uplift (Fig. 6).

2.3. Water level

We began in September 2016 to monitor water levels in the three wells (J6, J7, J10) at depths of 215, 204 and 171 m, respectively (Fig. 1a and 2b). Water levels are recorded with Solinst levellogger at a sampling rate of 1 h.

Decline of water level in the J6 well became perceptible when the workface was ~300 m away from the well (Fig. 4a, J6), but large decline of water level occurred when the workface was ~90 m from the well and water level reached a minimum when the workface was directly beneath the well (indicated by a red vertical dashed line), with a total head loss of ~20 m. After the workface passed away from the well, water level recovered and reached the pre-mining level in about half a month when the workface had moved >190 m away.

Decline of water level in the J7 well (Fig. 4a, J7) became perceptible when the workface was 712 m from the well; water level dropped sharply when the workface reached a distance of 300 m and was lowest when the workface was directly beneath the well (indicated by a red vertical dashed line), with a total head loss of ~44 m. Water level recovered rapidly after the workface passed the well. The borehole damaged and the well casing collapsed shortly after the workface passed the well; water level observations then ceased.

The changes of water level in the J10 well were distinct from those in the other two wells. Water level in the well began to decline only when the workface of panel 1229 was near the well; it continued to decline gradually long after the workface moved away. This is the only well that does not overlie an working panel.

2.4. Response to Earth tides

Tidal signals in the water level are small in magnitude and need to be extracted by applying Fourier analysis or some standard computer codes to the water-level time series. A widely used code in this aspect is Baytap based on a Bayesian inversion procedure (Tamura et al., 1991; Doan et al., 2006). Error analysis of the parameters is performed in the inversion with the conditional probability of the parameters knowing the data and its observational error. These are shown in Fig. 4 as error bars on each data point.

The amplitude ratio of the tidal response to the M₂ tide (Fig. 4b) shows a relatively simple pattern. In the J6 well, for example, this change resembles qualitatively the mirror image of the water level change (Fig. 4a). It began to slowly increase when the workface was ~300 m away; large increases occurred when the workface was fewer than ~150 m from the well and reached a maximum when the workface was directly beneath the well (Fig. 4b). When the workface moved away, amplitude decreased nearly symmetrically with distance from the maximum and returned to a small value when the work face was ~150 m away; it returned to the pre-excavation level when the workface passed by >~300 m.

The change of the phase shift in this well appears quite different from those of the water level and the amplitude ratio. It showed three minima, two maxima and several changes of signs during the course of this study (Fig. 4c). The initial phase shift was ~+10° when the workface was far away. It started to decrease when the workface was ~530 m from the well, reaching its first minimum of ~−40° when the workface was ~330 m away, at which a sudden increase occurred and reached its first maximum of ~+100° without a corresponding change of water level (Fig. 4a) or ground deformation in the satellite image (Fig. 4d). The phase shift stayed at this value until the workface was ~150 m away when it dropped to the second minimum of ~−70° within a short distance and stayed at this minimum until the workface advanced beyond the well to a distance of ~90 m away. It then rose within a short distance to the second maximum of ~+70° and stayed at this maximum until the workface moved to a distance of ~300 m from the well, where the phase shift dropped suddenly and decreased to the third minimum of ~−40°. It stayed at this value until the workface was at a distance ~640 m away;

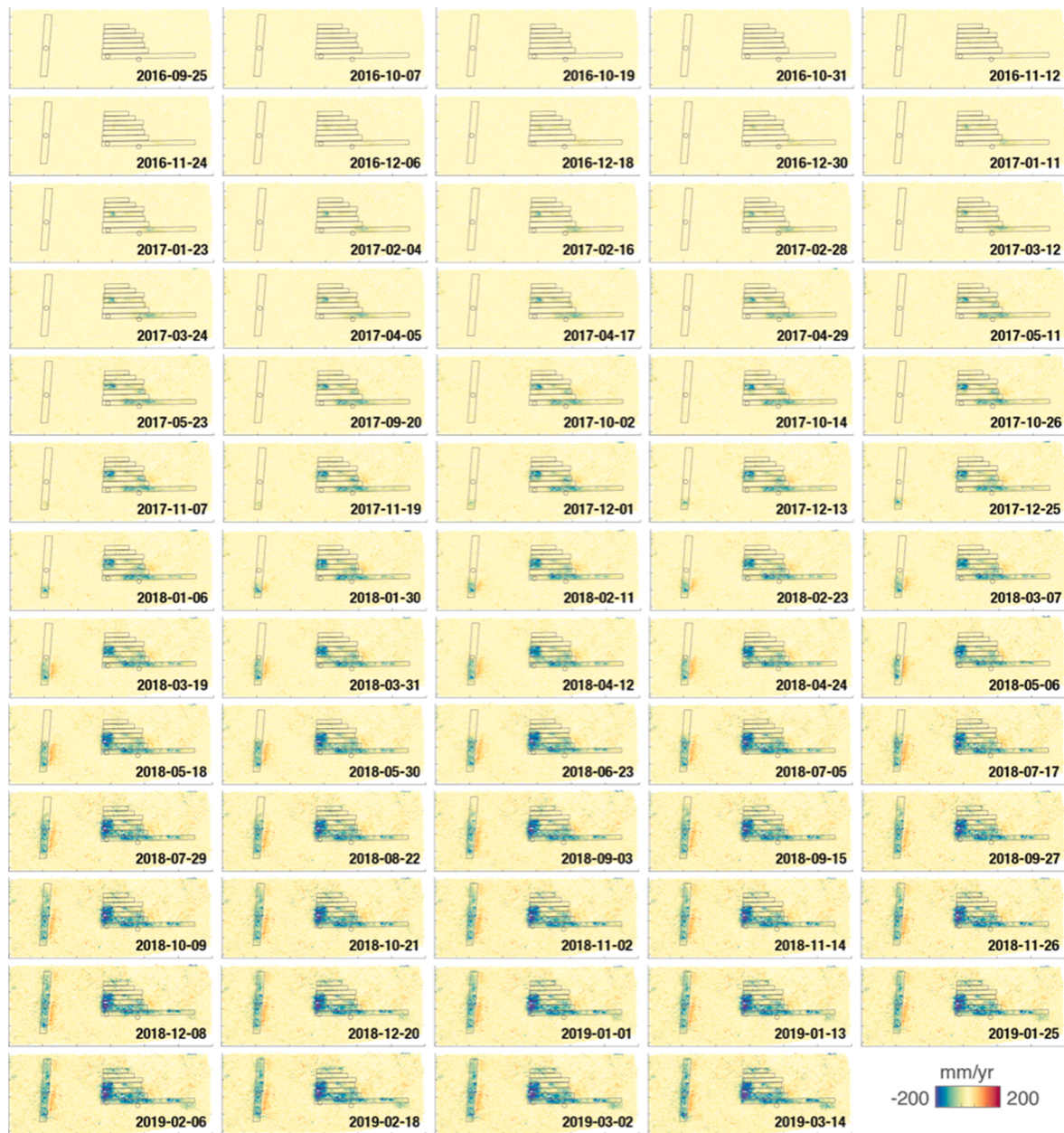


Fig. 5. Cumulative vertical displacement from 2016 to 2019.

it then rose, again without perceptible water-level change (Fig. 4a) or ground deformation in the satellite image (Fig. 4d), to the pre-excavation level of $\sim +10^\circ$.

The phase shift in the J7 well (Fig. 4c, J7) was stable near -40° when the workforce was far from the well. A significant decrease occurred when the workforce was still ~ 1.5 km away; it reached a minimum of $\sim -70^\circ$ and then slowly increased and accelerated to a maximum of $\sim 20^\circ$ when the workforce was ~ 400 m away. It dropped to a minimum of $\sim -50^\circ$ when the workforce was beneath the well. It increased to a second maximum when the workforce moved away, and the wellbore was damaged.

The tidal response of water level in the J10 well differs considerably from those in the other two wells. The amplitude ratio shows little change during surface subsidence (Fig. 4b, J10). The phase shift (Fig. 4c, J10), on the other hand, decreased significantly when the workforce in the 1229 panel was 345 m away. It increased to a maximum when the workforce met the well. After the workforce moved away, the phase shift decreased and fluctuated before returning to the pre-mining level.

3. Discussion

Many studies have used simple models to interpret the tidal response of groundwater in wells (Doan et al., 2006; Elkhoury et al., 2006). The present study, however, differs from these studies in two major aspects. First, the geology of mining areas is modified by the numerous fractures generated by the past and ongoing mining processes (e.g., Booth, 2002), which may alter the hydrology and dominate the tidal response of groundwater in mining areas (Zhang and López, 2019). The available simple models are constructed for horizontal aquifers and are thus inadequate for the interpretation of the tidal response of groundwater in the present study. Even though Hanson and Owen (1982) and Bower (1983) related tidal response to fractures, their models only account for the tidal response of groundwater in an isolated plane fracture, which is obviously far from the situation encountered in underground mining areas where the wall rocks are crisscrossed by multisets of intersecting, high-angle fractures (e.g., Booth, 2002). Second, the results of the tidal analysis are usually expressed as the phase shift with respect to the tidal

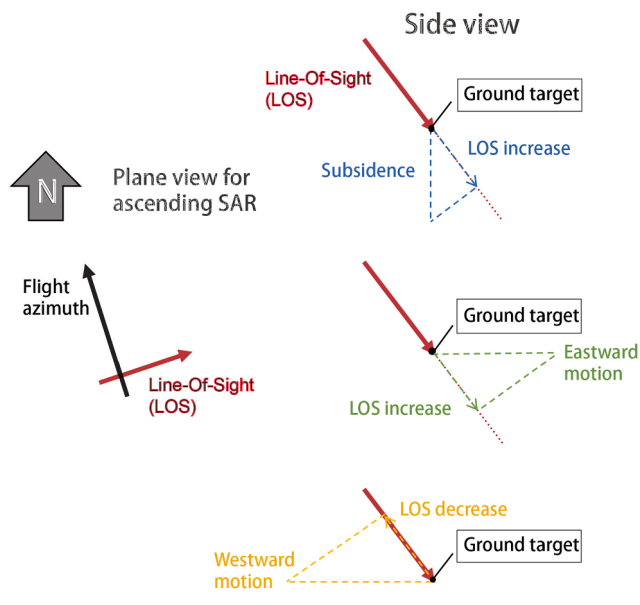


Fig. 6. InSAR geometry.

strain and the amplitude ratio of the water tides to the equivalent tidal pressure head. Because direct measurement of the tidal strains is unavailable in most wells, as in the presence case, the theoretical tidal strain at the well is assumed as the reference in the analysis. However, tidal strains are known to be significantly affected by the local geology (Beaumont and Berger, 1975), cavity and topography (Harrison, 1974). The numerous subsurface tunnels beneath the studied area may affect the local tidal strain in significant but unpredictable ways. As a consequence, the theoretical strain cannot serve as an accurate reference for the tidal analysis in the present study. For these reasons, only a qualitative interpretation of the tidal response may be attempted with the existing models. In spite of these difficulties, the present study is still a valuable contribution because it presents the first detailed report of the tidal response of groundwater in an actively and intensely mined area.

The large distances between the wells and the workface (~ 530 m for the J6 well and ~ 1500 m for the J7 well) when the first significant change of the phase shift to the M_2 tide occurred may appear surprising in view of previous studies of mining-induced microseismicity (e.g., Cheng et al., 2019) and stress changes (e.g., Meng et al., 2016), which showed a much smaller threshold distance. The comparatively large distance between the well and the workface when the first significant change of the phase shift occurred may be due to a combination of the sensitivity of the phase shift of the tidal response to minute stress changes in the shallow crust and to the effect of dynamic stresses in the seismic waves from small earthquakes (e.g., Brodsky et al., 2003; Manga and Wang, 2015). Small earthquakes are ubiquitous during coal mining (e.g., Arabasz et al., 2005; Cheng et al., 2019). However, few seismographs have been set up near the studied area because it is located inside a geologically stable craton (the Erdos craton) where few natural earthquakes have occurred or may be expected, and because no seismograph has been specifically set up for monitoring the mining-induced seismicity. The nearest seismic stations for monitoring the natural seismicity is ~ 30 km away. As a result, the accuracy for the epicentral locations is low and none of the eleven reported mining-induced earthquakes (with magnitude larger than 2.5) was located within the studied area during the studied period. For this reason, we cannot provide any detailed analysis of the seismic energy density from the induced seismicity or the earthquake-induced increase in permeability for this study. On the other hand, we may expect abundant, unreported small earthquakes in the mined area during the mining process, which would cause dynamic stresses that attenuate much more slowly with distance than the quasi-static stresses (Kilb et al., 2002; Brodsky et al., 2003).

Such dynamic stresses have been shown to be effective to mobilize the precipitates in clogged fractures and to increase the fracture permeability, which in turn may change the fracture permeability and the phase shift of the tidal response at large distances (e.g., Elkhoury et al., 2006).

The large increase of the amplitude ratio in the J6 and J7 wells (Fig. 4b, J6, J7) and simultaneous decline of water level (Fig. 4a, J6, J7) when the workface came near and beneath the wells contradicts the prediction of the porous flow models with a horizontal layer (Roeloffs, 1996; Doan et al., 2006; Wang et al., 2018). This may be because mining produces high-angle fractures in the wall rocks (e.g. Booth, 2002), which are likely to dominate the tidal response of groundwater. The tidal response in mining areas is also complicated by distortions of the strain field and the gravitational potential (e.g., King and Bilham, 1973; Beaumont and Berger, 1975). In addition, the drastic displacement identified on the interferograms (Fig. 4d, J7) in late August 2017, implies faulting-related mass movement that may further distort the local potential fields. On the other hand, the detailed recording of the time-dependent changes of tidal response may be explored to reveal a degree of qualitative understanding.

The most revealing aspect in the time-dependent change of tidal response is the sudden switches of sign in the phase shift, as described in the last section. Also highly revealing is the co-occurrence of the amplitude ratio maximum and the groundwater level minimum. The latter clearly indicates a great increase in the vertical permeability, which in turn implies the formation of vertical fractures or faults beneath the wells. None of the existing horizontal layered models can explain these changes, and thus we seek fracture models for explanation.

Bower (1983) showed, for fractures that incline at an angle to the horizon, the sign of the phase shift depends on the strike of the fracture plane. For a well located at a latitude of 45°N , for example, the phase shift of the tidal response to the M_2 tide is positive for fractures with strike (measured from the north) between 0° and 90° and negative for fractures with strike between 90° and 180° . With fracture dips increasing beyond 10° to 20° , the absolute phase shift decreases rapidly, while the amplitude increases more gradually. Therefore, the sharp switches of the signs of the phase shift with and the different characteristics between the phase shift and the amplitude ratio during the progressive mining and excavation are more consistent with the fracture model than the horizontal aquifer models. Even though the presence in the studied area of multiple intersecting sets of fractures with different strikes precludes a quantitative application of the fracture model, some qualitative suggestions may be made. Given the changing stress conditions in the mining area with the progression of the workface, it is reasonable to suggest that different sets of fractures are activated at different times, which, in turn, may have caused the rapid switching of the signs of the phase shift during the progress of mining. The observed rapid decline of water level and pronounced increase of the amplitude ratio in the J6 and the J7 wells when the workface comes close to and beneath the wells (Fig. 4a, b) are consistent with field observations that large fractures with steep dips form above excavated panels (David et al., 2017). Furthermore, faulting may occur near the well when the workface comes close, as suggested by the drastic displacement identified on the interferograms (Fig. 4d, J7) in late August 2017. The occurrence of steep fractures and faults may drastically increase the vertical leakage of the aquifer and change the sign of the phase shift (Bower, 1983).

The recovery of the water level and its tidal response at the J6 well after the workface moved away (Fig. 4a, b, c, J6) suggests that the permeability of the shallow crust recovered near the wells, which in turn suggests that the deviatoric stresses in the wall rocks were released, which allows the conductive narrow fractures to close and the permeability to return.

As noted earlier, the amplitude ratio of the tidal response of water level in the J10 well barely changed when the workface approached the well, even though the phase shift showed substantial changes. This

contrast illustrates that the phase shift is sensitively to relatively small stress changes, but the amplitude ratio is not. The groundwater level in this well declined continuously with time disregard to the progress of mining, in contrast with the situations in J6 and J7 wells, where the groundwater level showed a pronounced decline to a minimum when the workface arrived directly beneath the well, and then rose with time when the workface moved away. We hypothesize that the small responses of the groundwater level and the amplitude ratio in the J10 well are indicative that no steep fractures formed beneath the well during mining. As a result, the deviatoric stresses in the wall rocks were not released and the fractures and permeability did not recover, which allows the continued, gradual decline of water level in the J10 well long after the excavation activity in the nearby panel stopped.

4. Concluding remarks

We present in this study detailed analysis of the tidal response of groundwater and surface deformation from radar remote sensing in an actively and intensely mined area and show that the phase shift of the response of water level to Earth tides may be a more sensitive indicator than the other indicators to mining-induced disturbances on the hydro-mechanical state in the shallow crust. We hypothesize that mining-produced quasi-static and dynamic stresses may induce conductive fractures to open at large distance from the workface, which can significantly alter the tidal response of water level but cause little noticeable ground deformation and water level change. Large ground deformation and rapid decline in water level occur only under large deviatoric stresses when the workface comes much closer to the wells. The recovery of the water level and its tidal response after the workface moves away is more difficult to explain. We suggest that the occurrence of faulting during mining may have released the deviatoric stresses in the wall rocks to allow the conductive fractures to close and become non-conductive, allowing the permeability and the tidal response of the shallow crust to recover. Alternatively, mining induced seismicity around the coal field cause the permeability increase and recovery. More investigations are needed to better understand hydro-mechanical coupling during longwall mining.

CRediT authorship contribution statement

Zheming Shi: Methodology, Software, Writing - original draft, Data curation, Funding acquisition. **Xie Hu:** Formal analysis, Software, Writing - review & editing. **Chi-Yuen Wang:** Conceptualization, Writing - review & editing, Supervision.

Declaration of Competing Interest

The authors declare that they have no known competing financial interests or personal relationships that could have appeared to influence the work reported in this paper.

Acknowledgments

We thank the Xiangyang Liang and Shen Qu for their help during the field work and data collection. This work is partly supported by the National Key R&D Program of China (2018YFC0406401-1) to Z.M.S and the National Science Foundation grant EAR1344424 to C.Y.W. Sentinel-1 SAR data can be downloaded from Copernicus Open Access Hub and Alaska Satellite Facility.

References

- Adhikary, D., Guo, H., 2015. Modelling of longwall mining-induced strata permeability change. *Rock Mech. Rock Eng.* 48, 345–359.
- Arabasz, W., et al., 2005. Coal-mining seismicity and ground-shaking hazard: a case study in the Trail Mountain area, Emery County, Utah. *Bull. Seismol. Soc. Am.* 95 (1), 18–30.
- Armand, G., Leveau, F., Nussbaum, C., de La Vaissiere, R., Noiret, A., Jaeggi, D., Landrein, P., Righini, C., 2014. Geometry and properties of the excavation-induced fractures at the Meuse/Haute-Marne URL drifts. *Rock Mech. Rock Eng.* 47, 21–41.
- Bai, M., Elsworth, D., 1995. Influence of mining geometry on mine hydro-geo-mechanics. *Transactions 296.*
- Beaumont, C., Berger, J., 1975. An analysis of tidal strain observations from the United States of America: I. The laterally homogeneous tide. *Bull. Seismol. Soc. Am.* 65, 1613–1629.
- Brodsky, E.E., Roeloffs, E., Woodcock, D., Gall, I., Manga, M., 2003. A mechanism for sustained groundwater pressure changes induced by distant earthquakes. *J. Geophys. Res.* 108 (B8), 2390. <https://doi.org/10.1029/2002JB002321>.
- Booth, C.J., 2002. The effects of longwall coal mining on overlying aquifers. *Geological Society, London, Special Publications* 198, 17–45.
- Booth, C.J., Spande, E.D., 1992. Potentiometric and aquifer property changes above subsiding longwall mine panels, Illinois basin coalfield. *Groundwater* 30, 362–368.
- Bower, D.R., 1983. Bed rock fracture parameters from the interpretation of well tides. *J. Geophys. Res.* 88, 5025–5035.
- Cheng, G., et al., 2019. Microseismic investigation of mining-induced brittle fault activation in a Chinese coal mine. *Int. J. Rock Mech. Min. Sci.* 123, 104096.
- David, K., Timms, W., Barbour, L., Mitra, R., 2017. Tracking changes in the specific storage of overburden rock during longwall coal mining. *J. Hydrol.* 553.
- Doan, M.-L., Brodsky, E.E., Prioul, R., Signer, C., 2006. Tidal analysis of borehole pressure-A tutorial, University of California, Santa Cruz. Schlumberger Research Report.
- Day, M., Kos, P., Brinton, S., 2020. Hydrogeologic characterization and mining impact analysis of a low-yield, fractured granite. *Mining Metal. Explor.* 1–20.
- Ding, W., Peng, D., Zhu, D., Zhang, Y., He, J., Li, A., Wang, R., et al., 2016. Fractures in continental shale reservoirs: a case study of the Upper Triassic strata in the SE Ordos Basin, Central China. *Geol. Magazine* 153 (4), 663–680.
- Elkhouri, J.E., Brodsky, E.E., Agnew, D.C., 2006. Seismic waves increase permeability. *Nature* 441, 1135–1138.
- Feng, M.-M., Mao, X.-B., Bai, H.-B., Miao, X.-X., 2007. Analysis of water insulating effect of compound water-resisting key strata in deep mining. *J. China Univ. Mining Technol.* 17, 1–5.
- Hanson, J. M., & Owen, L. B. (1982). Fracture orientation analysis by the solid Earth tidal strain method, Soc. Pet. Eng. AIME Pap., SPE11070. <https://doi.org/10.2118/11070-MS>.
- Harrison, J.C., 1974. Cavity and topography effects on the measurement of tilt and strain. *EOS. Trans. Am. Geophys. Union* 56, 1151.
- Hu, X., Bürgmann, R., Schulz, W., Fielding, E., 2020. Four-dimensional surface motions of the Slumgullion landslide and quantification of hydrometeorological forcing. *Nat. Commun.*
- Hu, X., Lu, Z., Wang, T., 2018. Characterization of hydrogeological properties in Salt Lake Valley, Utah, using InSAR. *J. Geophys. Res. Earth Surf.* 123, 1257–1271.
- Hu, X., Oommen, T., Lu, Z., Wang, T., Kim, J.W., 2017. Consolidation settlement of Salt Lake County tailings impoundment revealed by time-series InSAR observations from multiple radar satellites. *Remote Sens. Environ.* 202, 199–209.
- Huang, X., Wang, G., Liang, X., Cui, L., Ma, L., Xu, Q., 2018. Hydrochemical and stable isotope (δD and $\delta^{18}\text{O}$) characteristics of groundwater and Hydrogeochemical processes in the Ningtaota coalfield, Northwest China. *Mine Water Environ.* 37, 119–136.
- Jung, H.C., Kim, S.-W., Jung, H.-S., Min, K.D., Won, J.-S., 2007. Satellite observation of coal mining subsidence by persistent scatterer analysis. *Eng. Geol.* 92, 1–13.
- Kilb, D., Gomberg, J., Bodin, P., 2002. Aftershock triggering by complete Coulomb stress changes. *J. Geophys. Res.* 107 (B4), 2060. <https://doi.org/10.1029/2001JB000202>.
- King, G., Bilham, R., 1973. Tidal tilt measurement in Europe. *Nature* 243 (5402), 74–75.
- Liu, J., Elsworth, D., 1997. Three-dimensional effects of hydraulic conductivity enhancement and desaturation around mined panels. *Int. J. Rock Mech. Min. Sci.* 34, 1139–1152.
- Manga, M., Wang, C.-Y., 2015. *Earthquake Hydrology*. Treatise on geophysics. Elsevier, Amsterdam.
- McNally, G., Evans, R., 2007. Impacts of longwall mining on surface water and groundwater, Southern Coalfield NSW. Report prepared for NSW Department of Environment and Climate Change. eWater Cooperative Research Centre: Canberra.
- Meng, Z., Shi, X., Li, G., 2016. Deformation, failure and permeability of coal-bearing strata during longwall mining. *Eng. Geol.* 208, 69–80.
- Roeloffs, E.A., 1996. Poreelastic techniques in the study of earthquake related hydrologic phenomena. *Adv. Geophys.* 37, 135–195.
- Sheng, Y., Ge, L., Rizos, C., Wang, Y., 2010. Monitoring underground coal mining-induced subsidence.
- Shirzaei, M., Ellsworth, W.L., Tiampo, K.F., González, P.J., Manga, M., 2016. Surface uplift and time-dependent seismic hazard due to fluid injection in eastern Texas. *Science* 353, 1416–1419.
- Stephansson, O., 2003. Theme issue on hydromechanics in geology and geotechnics. *Hydrogeol. J.* 11, 3–6.
- Tamura, Y., Sato, T., Ooe, M., Ishiguro, M., 1991. A procedure for tidal analysis 73 17 with a Bayesian information criterion. *Geophys. J. Int.* 104, 507–516.
- Wang, C.-Y., Doan, M.-L., Xue, L., Barbour, A.J., 2018. Tidal response of groundwater in a leaky aquifer—application to Oklahoma. *Water. Resour. Res.* 54 <https://doi.org/10.1029/2018WR022793>.
- Xue, C., Chi, G., Xue, W., 2010. Interaction of two fluid systems in the formation of sandstone-hosted uranium deposits in the Ordos Basin: geochemical evidence and hydrodynamic modeling. *J. Geochem. Explor.* 106.

- Zhai, G., Shirzaei, M., Manga, M., Chen, X., 2019. Pore-pressure diffusion, enhanced by poroelastic stresses, controls induced seismicity in Oklahoma. *Proc. Natl. Acad. Sci.* 116, 201819225.
- Zhang, D., Fan, G., Liu, Y., Ma, L., 2010. Field trials of aquifer protection in longwall mining of shallow coal seams in China. *Int. J. Rock Mech. Min. Sci.* 47, 908–914.
- Zhang, Q., López, D.L., 2019. Use of time series analysis to evaluate the impacts of underground mining on the hydraulic properties of groundwater of Dysart Woods, Ohio. *Mine Water Environ.* 38, 566–580.